MARTIN MARIETTA ENERGY SYSTEMS LIBRARIES
3 4456 0313699 7

ENERGY CONSERVATION

ORNL/Sub/86-SA578/1

Free-Piston Stirling Engine Magnetically Coupled Heat Pump: Critical Component Evaluation

Phase I Final Report

G. Chen

Report Prepared by

SUNPOWER, INC.
6 Byard Street
Athens, Ohio 45701

under
Subcontract 86X-SA578V

for the

ENERGY DIVISION
OAK RIDGE NATIONAL LABORATORY

operated by
MARTIN MARIETTA ENERGY SYSTEMS, INC.

for the
U.S. DEPARTMENT OF ENERGY
OFFICE OF BUILDINGS
AND COMMUNITY SYSTEMS

OAK RIDGE NATIONAL LABORATORY
CENTRAL RESEARCH LIBRARY
CIRCULATION SECTION
4500N ROOM 175
LIBRARY LOAN COPY
DO NOT TRANSFER TO ANOTHER PERSON
If you wish someone else to see this report, send in name with report and the library will arrange a loan.
UCN-7969 (3 9-77)

This report has been reproduced directly from the best available copy.

Available to DOE and DOE contractors from the Office of Scientific and Technical Information, P.O. Box 62, Oak Ridge, TN 37831; prices available from (615) 576-8401, FTS 626-8401.

Available to the public from the National Technical Information Service, U.S. Department of Commerce, 5285 Port Royal Rd., Springfield, VA 22161.
NTIS price codes—Printed Copy: A04 Microfiche A01

This report was prepared as an account of work sponsored by an agency of the United States Government. Neither the United States Government nor any agency thereof, nor any of their employees, makes any warranty, express or implied, or assumes any legal liability or responsibility for the accuracy, completeness, or usefulness of any information, apparatus, product, or process disclosed, or represents that its use would not infringe privately owned rights. Reference herein to any specific commercial product, process, or service by trade name, trademark, manufacturer, or otherwise, does not necessarily constitute or imply its endorsement, recommendation, or favoring by the United States Government or any agency thereof. The views and opinions of authors expressed herein do not necessarily state or reflect those of the United States Government or any agency thereof.

ORNL/Sub/86-SA578/1
Dist. Category UC-95d

Free-Piston Stirling Engine Magnetically Coupled Heat Pump: Critical Component Evaluation

Phase I Final Report

G. Chen

Report Prepared by
SUNPOWER, INC.
6 Byard Street
Athens, Ohio 45701

under
Subcontract 86X-SA578V
for the
ENERGY DIVISION
OAK RIDGE NATIONAL LABORATORY
Oak Ridge, Tennessee 37831
Operated by
MARTIN MARIETTA ENERGY SYSTEMS, INC.
for the
U. S. DEPARTMENT OF ENERGY
under contract DE-AC05-840R21400

Date Published - August 1989

MARTIN MARIETTA ENERGY SYSTEMS LIBRARIES
3 4456 0313699 7

ACKNOWLEDGMENTS

The author wishes to acknowledge the support provided to this program by the technicians and engineers of Sunpower, Inc., and the program management of DOE/ORNL. Special acknowledgment goes to W.T. Beale of Sunpower, Inc., and G.T. Privon and F.C. Chen of Oak Ridge National Laboratory for their guidance in this program.

4-0712

ABSTRACT

The Free-Piston Stirling Engine (FPSE) Magnetically Coupled Heat Pump Program at Sunpower involves the development of a FPSE/magnetic coupling/compressor (FPSE/MC/C) assembly for a gas residential heat pump application. The objectives of Phase I were (1) to evaluate the feasibility and characteristics of critical components such as a linear magnetic coupling and hermetic sealing, (2) to demonstrate through tests the performance of a magnetic coupling/compressor assembly, and (3) to evaluate the system concept design by applying an air-charged FPSE.

An axial coupling made of permanent magnets with improved magnetic strength and lowered cost, such as neodymium iron, has been considered a potential link to transmit power from a FPSE to a refrigerant compressor with hermetic sealing in this type of heat pump. During Phase I, analyses regarding the magnetic-coupling characteristics were performed. A motor/magnetic coupling/double-acting compressor test rig with a stainless steel pressure shell was designed, fabricated, and tested. With the compressor loaded by air, the test rig successfully operated at various frequencies. Based on Sunpower's 3 kW air-charged FPSE concept, a FPSE/MC/C assembly conceptual design has been established. In addition, a system with an engine specifically redesigned for the heat pump application is under consideration.

The static force-deflection function of a test magnetic coupling, predicted from an analytical model and experimental measurements, showed close agreement. An optimal design of a magnetic coupling for specified permanent magnets can be created based on the model. The loss from the experimental magnetic coupling with the stainless steel shell within the gap running at 58 Hz was measured as 220 W to 347 W with the driven stroke ranging from 22 mm to 27 mm. Analytical calculations predicted the loss of a coupling crossing a stainless steel pressure vessel wall with the air-charged FPSE developed at Sunpower as about 6.3 percent of the transmitted power. The loss will be reduced by using a pressure shell made of material with high electrical resistivity. The ceramic test results indicated that the magnet temperature in operation was within the recommended range for neodymium iron.

The analytical and experimental results in the completed Phase I program have shown that the magnetic coupling is feasible and applicable for the FPSE-driven heat pump, which confirms the potential for further development of the FPSE magnetically coupled heat pump.

TABLE OF CONTENTS

SECTION		PAGE
	ACKNOWLEDGMENTS	ii
	ABSTRACT	iii
	LIST OF FIGURES	v
	LIST OF TABLES	vi
	NOMENCLATURE	vii
	SUMMARY	ix
1.0	INTRODUCTION	1
2.0	PERMANENT MAGNET COUPLING CONSIDERATIONS	5
	2.1 Selection of Magnet Material	5
	2.2 Magnetic Coupling Design	6
	2.3 System Resonant Characteristics	10
3.0	TESTS AND RESULTS	16
	3.1 Magnetic Coupling/Double-Acting Compressor Test Rig	16
	3.2 Tests and Result Analyses	23
	3.2.1 Magnets Exposed to R-22	23
	3.2.2 Force-Deflection Characteristic of the Experimental Coupling	23
	3.2.3 System Operation	26
	3.2.4 Power Loss in Magnetic Coupling	26
	3.2.5 Operating Temperature of Magnetic Coupling	31
	3.2.6 Irreversible Loss	33
	3.2.7 Rotational Force and Side Loading	35
4.0	FPSE/MAGNETIC COUPLING/COMPRESSOR ASSEMBLY	37
5.0	REFERENCES	41

LIST OF FIGURES

NUMBER		PAGE
1.1	Schematic of FPSE Magnetically Coupled Heat Pump (in Heating Mode)	2
2.1	Magnetic Coupling Configuration (a) Configuration (b) Alternating-Polarity Arrangement	7
2.2	Calculated Static Force of an Experimental Magnetic Coupling as a Function of its Deflection	9
2.3	Magnetic Coupling Loss as a Function of Electrical Resistivity of Pressure Vessel Material	11
2.4	Magnetic Coupling Loss as a Function of Average Coupling Linear Speed	12
2.5	Magnetic Coupling/Double-Acting Compressor System Resonant Characteristics (a) Simplified System (b) Force-Vector Diagram of Driven Component	13
3.1	Motor/Magnetic Coupling/Double-Acting Compressor Test Assembly	17
3.2	Test Rig with Instrumentation	18
3.3	Magnetic Coupling/Double-Acting Compressor Assembly of Test Rig	19
3.4	Coupling Components	21
3.5	Double-Acting Test Compressor	22
3.6	Force-Deflection Diagram of the Experimental Magnetic Coupling	25
3.7	Stainless Steel Shell Temperature within a Starting Period of the Test Rig Operation (58 Hz, 22 mm Driven Stroke)	28
3.8	Power Loss in the Experimental Magnetic Coupling	29
3.9	Predicted Power Loss in an Ideally Designed Magnetic Coupling to be Used for a 3 kW Engine with Various Strokes (Neodymium Iron; 2.5 MPa; G~3 mm)	30
3.10	Operating Temperature of Stainless Steel Shell in the Experimental Magnetic Coupling (58 Hz)	32
3.11	Static Force-Deflection Diagram of the Experimental Magnetic Coupling Before and After Operation	34
3.12	Predicted Radial Force of the Experimental Magnetic Coupling along with Eccentricity of Magnet Pairs (Static Condition)	36
4.1	Air-Charged FPSE/Magnetic Coupling/Compressor Assembly (Preliminary, 3kW)	38
4.2	Required Magnet Mass of a Coupling Linked to a Double-Acting Compressor (P=3 kW, G=3 mm, f=60 Hz, Neodymium Iron)	40

LIST OF TABLES

NUMBER		PAGE
2.1	Permanent Magnet Properties	5
3.1	Properties of Magnets in the Experimental Magnetic Coupling	16
3.2	Experimental Magnetic Coupling Specifications	20
3.3	Axial Force of the Test Magnetic Coupling as a Function of its Deflection	24
4.1	Assembly Design Specifications	37

NOMENCLATURE

A	area	m^2
B	magnetic flux density	Wb/m^2 (T)
B_r	magnet residual induction	Wb/m^2 (T)
c	damping constant	kg/s
c_c	compressor damping constant	kg/s
c_m	magnetic coupling damping constant	kg/s
c_p	power piston damping constant	kg/s
c_s	specific heat of the cylindrical shell between magnet rings	J / kg °C
d	axial gap between magnet rings	m
D	coupling diameter	m
F	magnetic coupling axial force	N
F_a	calculated axial force	N
F_m	measured axial force	N
F_p	engine driving force	N
F_r	radial force	N
f	system operating frequency	Hz
G	gap between inner and outer coupling rings	m
H_c	Coercive force	A/m
k_g	equivalent compressor gas spring effect	N/m
k_m	magnetic coupling spring effect	N/m
k_p	spring effect on power piston	N/m
k_s	added compensating spring constant	N/m
L	magnetic coupling length in its axial direction	m
m	mass	kg
m_p	power piston mass	kg
m_s	mass of the shell within coupling gap and swept by magnets	kg
N	the number of magnet pairs	
P	power	W
P_L	power loss in a magnetic coupling	W
Q_s	heat flow rate to surroundings	W
R	electrical resistivity	Ω cm
s	stroke	m
T	temperature	°C
T_c	magnet curie temperature	°C

T_s	stainless steel shell temperature	°C
t	time	s (min)
t_s	pressure vessel thickness in coupling gap	m
t_m	magnet thickness	m
t_b	iron thickness	m
U	overall heat transfer coefficient	W/m^2 °C
u	mean linear velocity of coupling	m/s
V	volume	m^3
w	magnet width	m
X_c	compressor piston amplitude	m
x	coupling deflection	m
x_c	compressor piston displacement	m
x_p	power piston displacement	m
ω	angular velocity	rad/s

SUMMARY

Phase I of the FPSE magnetically coupled heat pump program involved the critical component evaluation, analytically and experimentally. The analytical work focused on the study of characteristics of a permanent magnet coupling and magnetic coupling/ compressor resonant system.

The experimental work consisted of design, fabrication, and testing of a motor/crankshaft/magnetic coupling/double-acting compressor test rig. The tests primarily covered evaluation of the magnetic coupling characteristics, including its force-deflection relationship, power loss, irreversible loss, and operating temperature; exposing permanent magnets to R-22; and study of the magnetic coupling/reciprocating compressor system resonant characteristics. As an application, a FPSE/MC/C assembly applying Sunpower's 3 kW air-charged engine was considered.

The successfully performed Phase I work has shown a great potential for further development of the FPSE magnetically coupled heat pump. In summary, the following conclusions can be made from the tests, analysis, and preliminary assembly design.

1. Good understanding of the characteristics of a linear magnetic coupling with a coupling/compressor system has been achieved.

2. Magnetic coupling characteristics can be adequately predicted. The optimal design of a magnetic coupling can be effectively and easily created by applying classical electromagnetic theory.

3. The experimental magnetic coupling used in the test rig has a load capacity greater than 3 kW with the air-charged engine operating conditions. The magnet mass of a magnetic coupling for a certain power transmission can be reduced by increasing either the frequency or stroke, before this is done consideration must be given to the dynamic force requirements of starting and cycling.

4. The magnet mass can also be reduced as the applied load is reduced. The force acting on the magnetic coupling in a ideally designed system is only the compressor damping force. This must be considered in system design.

5. The driven stroke is variable along with the compressor loading since the coupling deflection between the driving and driven components varies along with the imposed coupling load. This system characteristic requires consideration of resonant system tuning over a wide range of operating conditions in system design.

6. The power loss from a magnetic coupling to be used in the 3 kW air-charged FPSE/coupling/compressor assembly with a stainless steel pressure shell is predicted as about 190 W which is 6.3 percent of 3 kW. A pressure vessel wall made of material with both high electrical resistivity and strength can greatly reduce the coupling loss. A search for such a material for this application is being conducted in this investigation.

7. Operating temperature of a magnetic coupling depends on not only the coupling loss but also heat transfer to the surroundings. The measured temperature of the test model was within the recommended operating temperature range of neodymium iron. The irreversible magnetization loss of neodymium iron magnets at the operating temperature is small. Reversible loss due to temperature rise should be taken into consideration in design.

8. Side load and rotational force are negligible within usual machining tolerances.

Consequently, the following recommendations are made based on the above conclusions.

1. A continuing program to evaluate and demonstrate the performance of a FPSE/MC/C assembly for the heat pump system is recommended.

2. In the further development of a FPSE/MC/C assembly, redesign of a free-piston Stirling engine specifically for the heat pump application is recommended. The new system should be competitive with existing electrically driven heat pumps.

1.0 INTRODUCTION

A free-piston Stirling engine (FPSE) with its advantage of multi-fuel capability, high efficiency, quiet operation, hermetic sealing, little side load, and low maintenance has been considered for application as a prime mover in a gas residential heat pump. In a FPSE-driven heat pump, the engine working fluid and refrigerant of the compressor need to be hermetically sealed from each other. The major effort in the critical component development of the FPSE-driven heat pump has focused on finding an effective and efficient means to transmit power from the engine to the compressor with hermetic sealing.

Previous attempts included the inertia compressor, the hydraulic diaphragm, and a direct shaft drive with sliding seals [1]. Each of these methods has drawbacks in the form of complex dynamic interactions, mechanical complexity, seal leakage, or cost. Another method to meet the requirements for the hermetically sealed FPSE-driven heat pump is to use the already-developed FPSE-linear alternator to drive a conventional electrically operated heat pump. The electric power produced in this system can be diverted for other uses, as well as for the heat pump. The cost of this electrical system relative to direct drives would probably be higher.

A FPSE-driven magnetically coupled heat pump has long been considered a potentially better system by Sunpower [2] [3]. Due to the improved energy product and lowered cost of permanent magnets such as neodymium iron, a linear magnetic coupling has become an attractive selection for power transmission in a FPSE-driven heat pump. The objectives of the completed Phase I work covered in this report were to evaluate the critical components, including the magnetic coupling and hermetic sealing, and to demonstrate by means of bench tests the performance of the magnetic coupling/compressor system.

A schematic of a magnetically coupled FPSE-driven heat pump is illustrated in Fig. 1.1 [2]. The power module of the system consists primarily of a free-piston

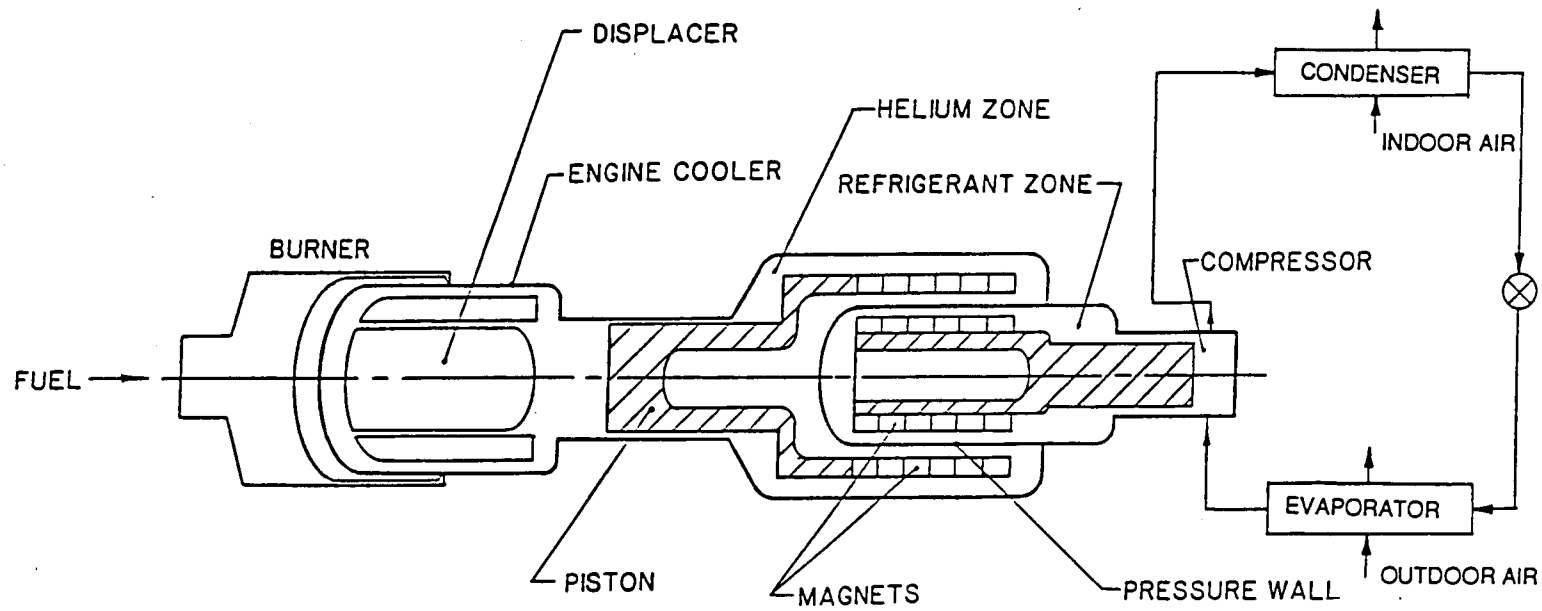

Figure 1.1 Schematic of FPSE Magnetically Coupled Heat Pump (in Heating Mode)

Stirling engine, a permanent magnet coupling, and a refrigerant compressor. For Rankine-cycle heat pump operation, an outdoor unit (the evaporator in heating mode), an indoor unit (the condenser in heating mode) and thermostatic expansion valve are also connected to the system to form a complete heat pump system. Thus, heat from outdoor air is absorbed by the low temperature refrigerant, raised to a higher temperature during the vapor compression by the engine work input to the compressor, and, finally, released for heating purposes. In the described system, power from the FPSE is transmitted to the refrigerant compressor through the magnetic coupling crossing the Stirling engine's pressure vessel wall. The pressure vessel wall between the magnets separates the working fluid of the Stirling engine from the refrigerant in the compressor. Compared with other FPSE-driven heat pump systems, this type of heat pump has the following advantages:

1. The magnetic coupling as a hermetic coupling eliminates mechanical contact between the engine power piston and compressor, and hermetically separates the engine working fluid and refrigerant. The coupling configuration is simple and the system assembly will be compact.

2. Within the intended range of operating conditions, the coupling will be free of mechanical degradation.

3. With proper design, the power loss in a magnetic coupling is low.

The completed Phase I work consists of:

1. Evaluation of the permanent magnet coupling characteristics and development of a magnetic coupling design methodology.

2. Investigation of the FPSE/magnetic coupling/compressor dynamic behavior.

3. Design, fabrication, and tests of a magnetic coupling/double-acting compressor assembly.

4. Conceptual assembly design based on the 3 kW air-charged FPSE developed at Sunpower.

2.0 PERMANENT MAGNET COUPLING CONSIDERATIONS

A linear permanent magnet coupling is a critical component in the development of this type of heat pump system. The magnetic coupling, with its basic configuration shown in Fig. 2.1, should be designed to maximize the force and stiffness per unit mass of the permanent magnets. The design effort evolved after considering the following:

1) Magnet material,
2) Design parameters, and
3) System resonant characteristics.

2.1 Selection of Magnet Material

Neodymium iron was considered an ideal permanent magnet for a magnetic coupling. Compared with samarium cobalt, neodymium iron has the following advantages:

1) Higher magnetic energy product,
2) Lower density,
3) Lower price, and
4) Higher resistance to chipping during handling.

Information in general about both neodymium iron and samarium cobalt is listed in Table 2.1.

Table 2.1 Permanent Magnet Properties [4] [5]

	Neodymium Iron	Samarium Cobalt
Peak Energy Product (kJ/m^3)	~280	~210
Density (g/cm^3)	~7.5	~8.2
Curie Temperature (°C)	~300	~800
Price* ($ /kg)	~90	~150

*Estimated from information provided by permanent magnet manufacturers

Because of the concern about magnet demagnetization with elevated temperature, the recommended operating temperature of neodymium iron is usually not higher than 130°C, based on its 300°C Curie temperature. The magnetic coupling connection to the power piston is typically located at the cold end of the FPSE. The heat to the magnets contained in a coupling is primarily from the magnetic coupling eddy-current loss.

To avoid demagnetization by overheating the magnets (in other words, to ensure the magnet temperature in operation will not exceed manufacturer recommendations), two issues need to be addressed. First, the magnetic coupling loss must be evaluated. Second, a system must be designed to keep the magnet operating temperature low. These issues will be described in Sections 2.2 and 3.2.4, respectively.

2.2 Magnetic Coupling Design

The design parameters of a magnetic coupling include the radial distance between the inner and outer coupling rings (G), the thickness of the magnet (t_m), the thickness of the iron base (t_b), the width of the magnet (w), the coupling diameter (D), and the number of magnetic pairs (N), all of which are shown in Fig. 2.1.

The essential goal for the design of a permanent magnet coupling is to achieve the required coupling load capacity with a minimum volume of permanent magnets, subject to existing design constraints. Based on this consideration, analytical work in Phase I concentrated on the development of a model that could predict the magnetic coupling load capacity represented by the axial coupling force (F) as a function of the coupling deflection (x) with specified coupling geometries and permanent magnet properties. From classical electromagnetic theory [6], the force may take a function as:

$$F = \mathbf{f}\,(x, N, G, w, t_m, t_b, d, D, B_r) \tag{2.1}$$

where d is the axial distance between magnet rings of the same row, and B_r is the magnetic residual induction.

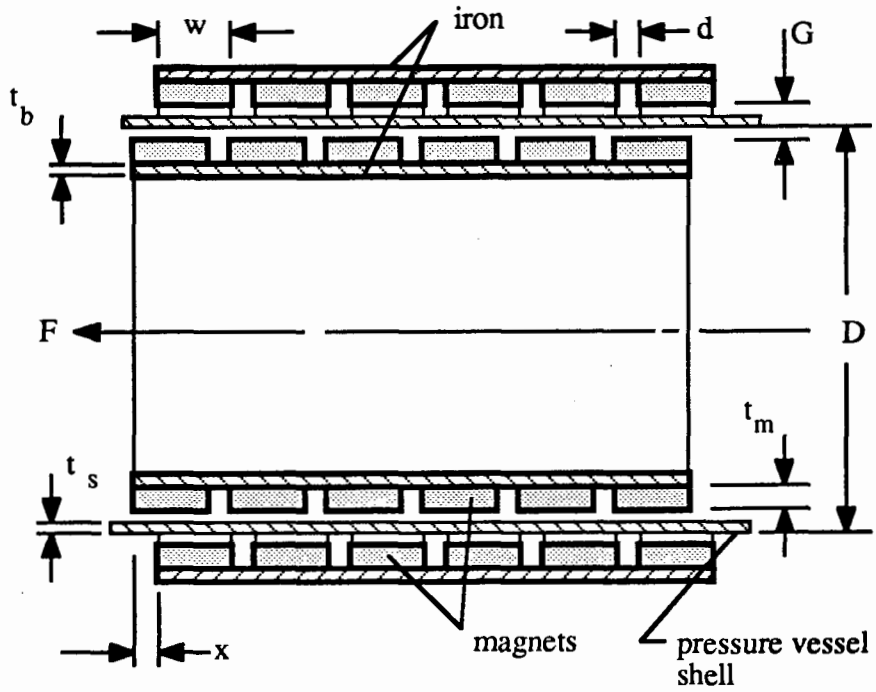

(a)

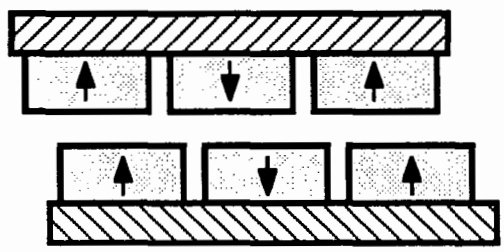

(b)

Figure 2.1 Magnetic Coupling Configuration

(a) Configuration (b) Alternating-Polarity Arrangement

The equations derived from the classical electromagnetic theory and corresponding computer programs to implement the determination of the design parameters are not included in this report.

The calculated force-deflection diagram of an experimental magnetic coupling used in the test rig is shown in Fig. 2.2. The comparison between results of the force-deflection characteristics from the analytical model and tests will be stated in Section 3.2. Geometries and sizes of a magnetic coupling for a given load capacity can be easily optimized by a design method based on the successfully developed model. It is noted that the maximum coupling load considered in a design is a point on the F-x curve with a positive stiffness, i.e., at $x<x|_{dF/dx=0}$. Obviously, the required magnet mass for a given load capacity will be less as the coupling operating point is moved closer to the instability point (dF/dx=0).

Arranging magnets of alternating polarity in a magnetic coupling (Fig. 2.1) causes identical surface currents of adjacent magnets at the magnet interface [6], which leads to a large restoring force and a stiff coupling. The distance, G, depends upon the thickness of the pressure vessel wall which can bear the engine internal pressure, and is usually a given parameter minimized to gain high power transmission. In general, a 300 type stainless steel shell with 100 mm diameter and 1.5 mm thickness is suitable for 2.5 MPa (25 bar), which is the mean internal working pressure in Sunpower's 3 kW air-charged engine. Since the pressure stresses are proportional to the diameter of the pressure vessel, the small diameter pressure vessels can be thinner, thus reducing the distance, G.

Power loss in a linear magnetic coupling is primarily caused by eddy current, i.e., by heat generated within the shell between the inner and outer magnet rings when the coupling is oscillating. According to classical electromagnetic theory [6], the loss (P_L) is a strong function of the permanent magnet strength (B_r), the coupling linear speed related to both the operating frequency (f) and coupling stroke (s), the electrical resistivity of the

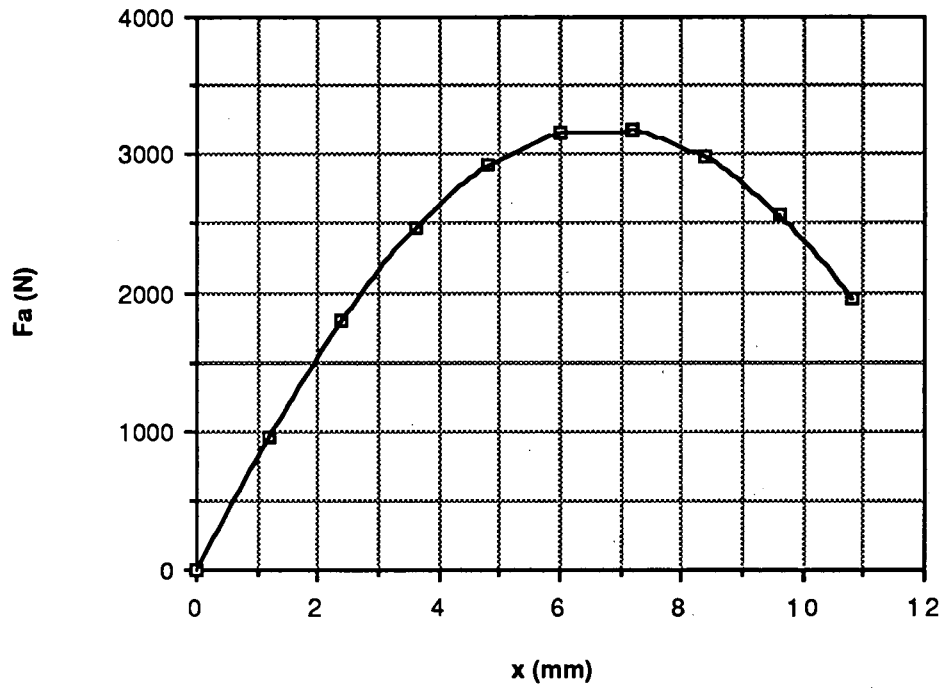

Figure 2.2 Calculated Static Force of an Experimental Magnetic Coupling as a Function of its Deflection

pressure vessel material (R), and the volume of the pressure vessel shell within the width of the total magnetic rings (V). The function may be expressed as:

$$P_L = (1/R)\ \{[(\pi / \sqrt{2})\ f\ s\ B_r\ t_m] / (G+2t_m)\}^2\ V \qquad (2.2)$$

It can be interpreted from the function above that two parameters have significant impact on reducing the coupling loss. One, as the electrical resistivity (R) of the pressure vessel material within the coupling gap is increased, the coupling power loss is rapidly decreased. The comparison of the loss in a fixed coupling/pressure vessel geometry as a function of R is shown in Fig. 2.3. Two, the loss varies proportionally to the product of the frequency and stroke ($f \times s$) as a coupling load capacity and G are fixed, as shown in Fig. 2.4. This can be derived from relationships (2.1) and (2.2) by considering that V is inversely proportional to ($f \times s$) when the coupling load capacity and G are given. Since the average speed ($2\ f \times s$) implies the term of ($f \times s$), the loss varies proportionally to the average coupling speed.

2.3 System Resonant Characteristics

The power module in this heat pump system primarily consists of a free-piston Stirling engine, a permanent magnet linear coupling, and a refrigerant compressor. The engine power piston, the magnetic coupling, and the compressor piston form a coupled resonant system. This system may be expressed by a simplified free-body diagram shown in Fig. 2.5 (a), where the mass, m_c, includes all the driven components, such as the outer magnet rings, compressor piston, and rod. The force-vector diagram on m_c is depicted in Fig. 2.5 (b). Since determination of the load capacity of a magnetic coupling depends upon the maximum force acting on the coupling, the design of a magnetic coupling and the power piston/magnetic coupling/reciprocating compressor system are also based on the characteristics of the system dynamics.

A double-acting reciprocating compressor was initially considered for application of this type of heat pump and for the Phase I test program. In the test program, a double-acting

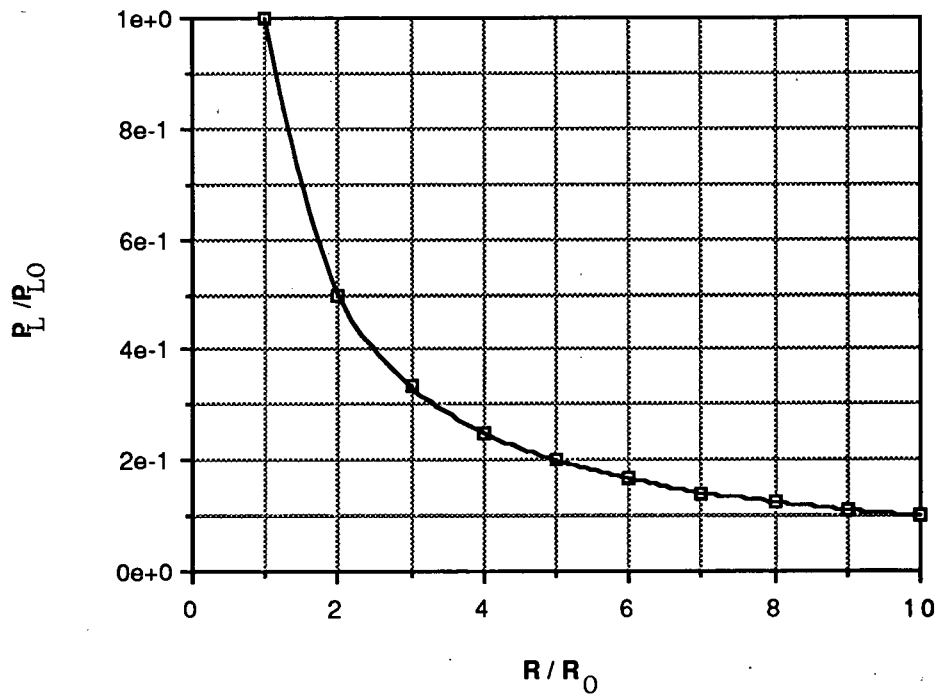

P_L - power loss

P_{L0} - power loss corresponding to R_0

R - electrical resistivity

R_0 - reference electrical resistivity

Figure 2.3 Magnetic Coupling Loss as a Function of Electrical Resistivity of Pressure Vessel Material

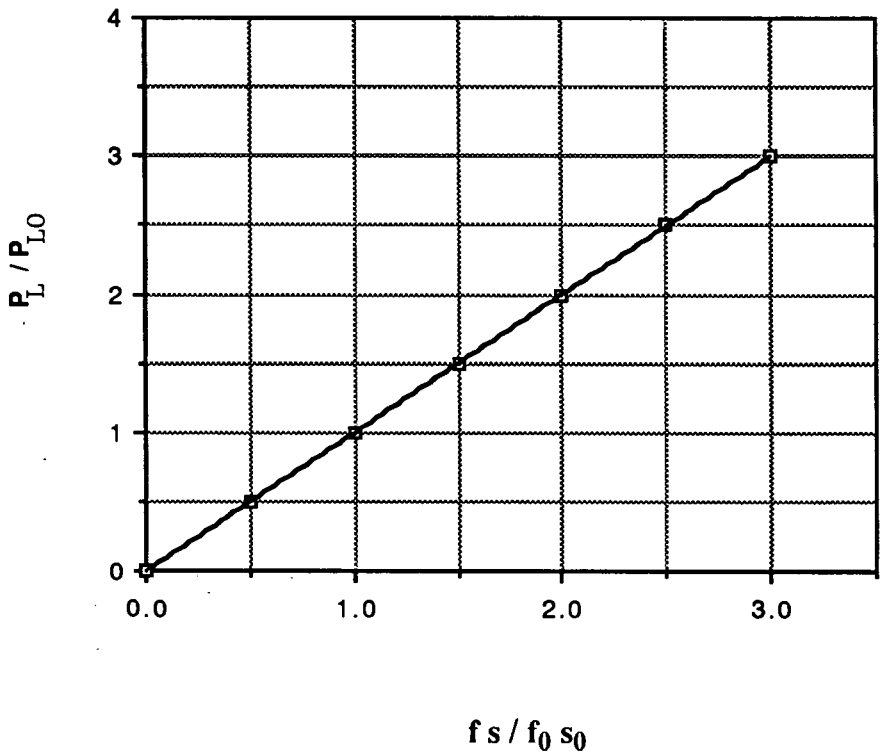

$(f_0\ s_0)$ - reference $(f\ s)$

P_L - power loss

P_{L0} - power loss corresponding to $(f_0\ s_0)$

Input power (P) and gap (G) are constants

Figure 2.4 Magnetic Coupling Loss as a Function of Average Coupling Linear Speed

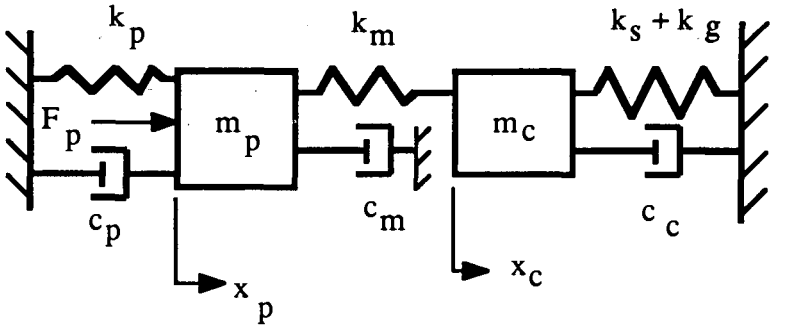

(a)

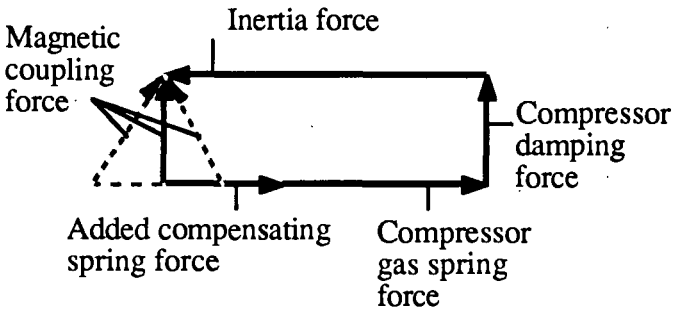

(b)

c_p	- damping constant of power piston
c_c	- damping constant of compressor
c_m	- damping constant of magnetic coupling (coupling loss)
F_p	- engine driving force
k_p	- spring effect on power piston
k_m	- magnetic coupling spring effect (nonlinear)
m_p & m_c	- mass of power piston and mass of driven components
k_s	- added compensating spring effect
k_g	- equivalent compressor gas spring effect (nonlinear)
x_p & x_c	- displacement of power piston and compressor piston

Figure 2.5 Magnetic Coupling/Double-Acting Compressor System Resonant Characteristics
(a) Simplified System (b) Force-Vector Diagram of Driven Components

reciprocating compressor was fabricated and used as a load to the experimental magnetic coupling. The maximum damping force of the double-acting compressor, shown in Fig. 2.5 (b), proportional to the compressor power absorption and inversely proportional to the frequency and piston stroke of the compressor, may be approximately calculated from:

$$F_{dmax} = 2P / \pi f s \tag{2.3}$$

where P = power required to drive the compressor
f = frequency
s = stroke

This relation was simply derived from a relationship of harmonic power and a sinusoidal motion. Since the damping force resulting in a power dissipation will not cancel, the force acting on the linear magnetic coupling for a fixed power transmission is minimized when the driven components are resonated. This means that in an ideally designed system, the only force which must be transmitted by the magnetic coupling is the damping force. By ignoring the coupling loss, the force acting on the magnetic coupling, $k_m x$, is minimized and equal to the damping force when the inertia effect is entirely balanced, thus minimizing the magnet mass. This can be seen in Fig. 2.5 (b). The analysis indicates the addition of springs on the driven components is required when the driving frequency is high.

It needs to be noted that, unlike a conventional mechanical link which connects the driving and driven parts rigidly, a magnetic coupling acts like a spring since the deflection between the driving and driven components varies along with the imposed load on the magnetic coupling (Fig. 2.2). The gas force on the compressor piston varies as the double-acting compressor is subjected to varying pressure and temperatures over the operating range of the heat pump. The system is balanced in inertia and in spring effects at one compressor operating pressure, but it will not be so at higher or lower pressures. This also means that the magnetic coupling with its spring characteristics requires

consideration of the resonant system tuning over a wide range of operating conditions in the system design.

In a resonant system, wherein the engine and compressor are tuned to the same frequency, the only force which must be transmitted by the magnetic coupling is the damping force. Hence, the running load capacity of a magnetic coupling can be simply evaluated from its force-deflection characteristics.

3.0 TESTS AND RESULTS

The tests performed on a magnetic coupling/double-acting compressor test rig were designed to evaluate the characteristics of the magnetic coupling and to demonstrate the performance of a magnetic coupling in a coupling/compressor system.

3.1 Magnetic Coupling/Double-Acting Compressor Test Rig

To perform the tests, a test rig (schematic shown in Fig. 3.1) was designed, fabricated, and tested. The test rig with auxiliary apparatus and instrumentation (illustrated in Fig. 3.2) basically consists of (1) a magnetic coupling/double-acting compressor assembly (shown in Fig. 3.3), (2) a 5 kW motor driving the test rig, and (3) a belt/pulley/crankshaft transmission converting rotation to linear motion. Varying the ratio in the transmission or the crank radius allowed for change in the operating frequency or in the coupling stroke, respectively. However, the crank radius was set as 12 mm (24 mm driven stroke) in the tests.

The magnetic coupling in the test assembly consisted of six pairs of rings made of pieces of neodymium iron with alternating polarities. Properties of the magnet can be found in Table 3.1.

Table 3.1 Properties of Magnets in the Experimental Magnetic Coupling [7]
(Neodymium Iron-Hicorex Nd 94 EB from Hitachi)

Residual Induction, B_r (Wb/m^2)	1.1 to 1.2
Coercive Force, H_c (A/m)	804×10^3 to 891.5×10^3
Energy Product , $(BH)_{max}$ (kJ/m^3)	224 to 272
Curie Temperature, T_c (°C)	300
Reversible Temp. Coeff. of Magnetization (%/°C)	-0.109
Density (g/cm^3)	7.5
Recommended Operating Temperature (°C)	-40 to +125

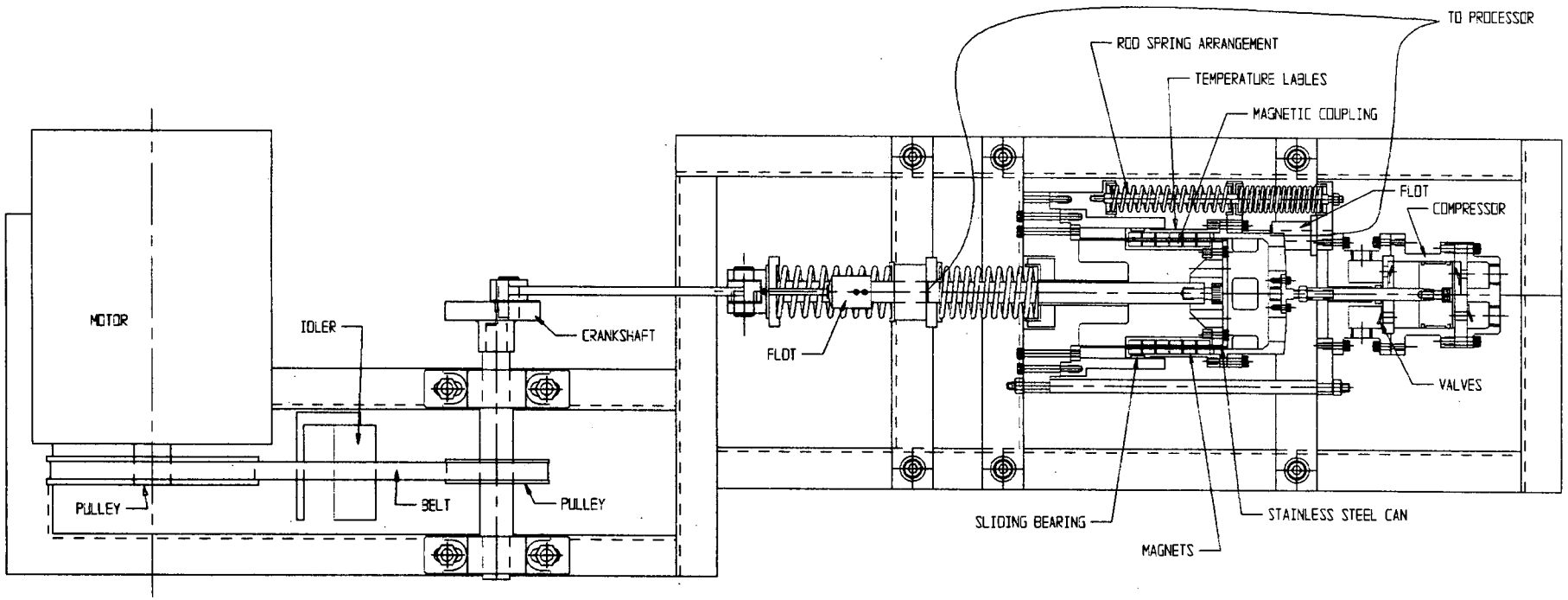

Figure 3.1 Motor/Magnetic Coupling/Double-Acting Compressor Test Assembly

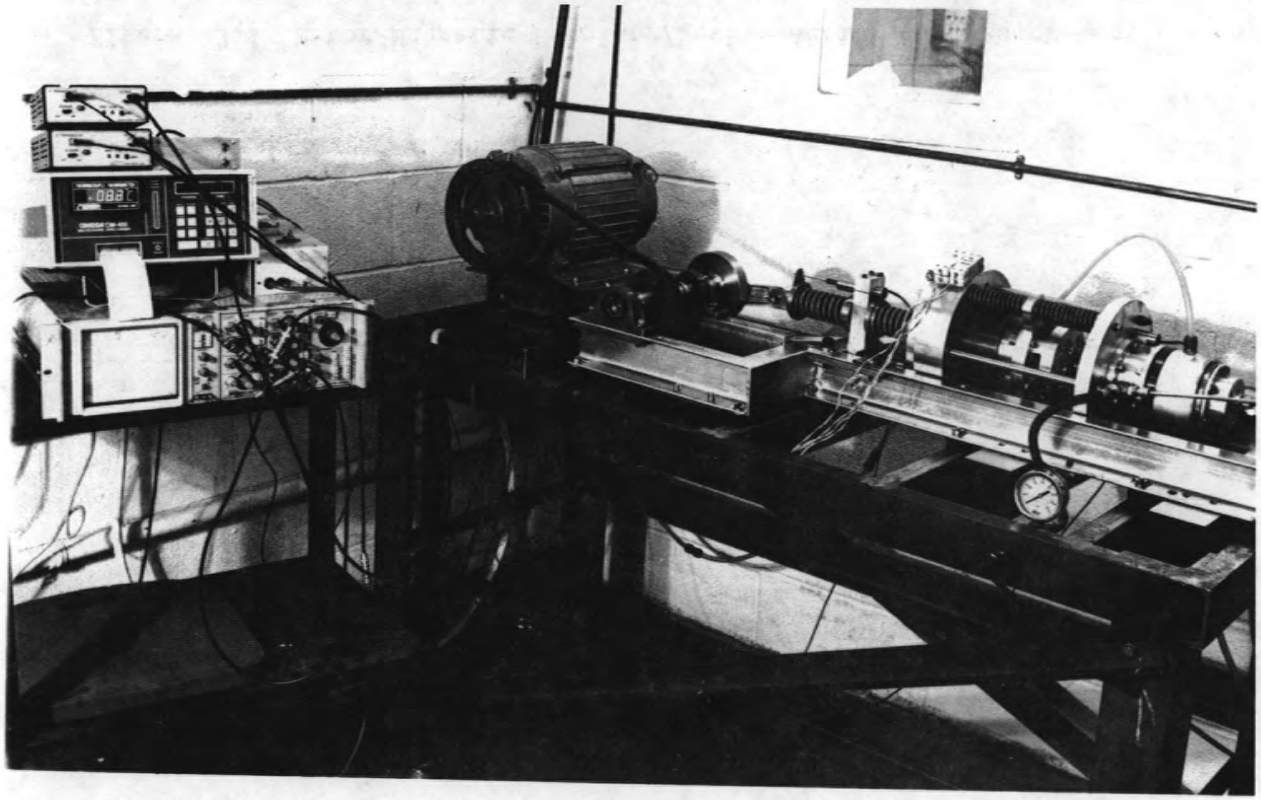

Figure 3.2 Test Rig with Instrumentation

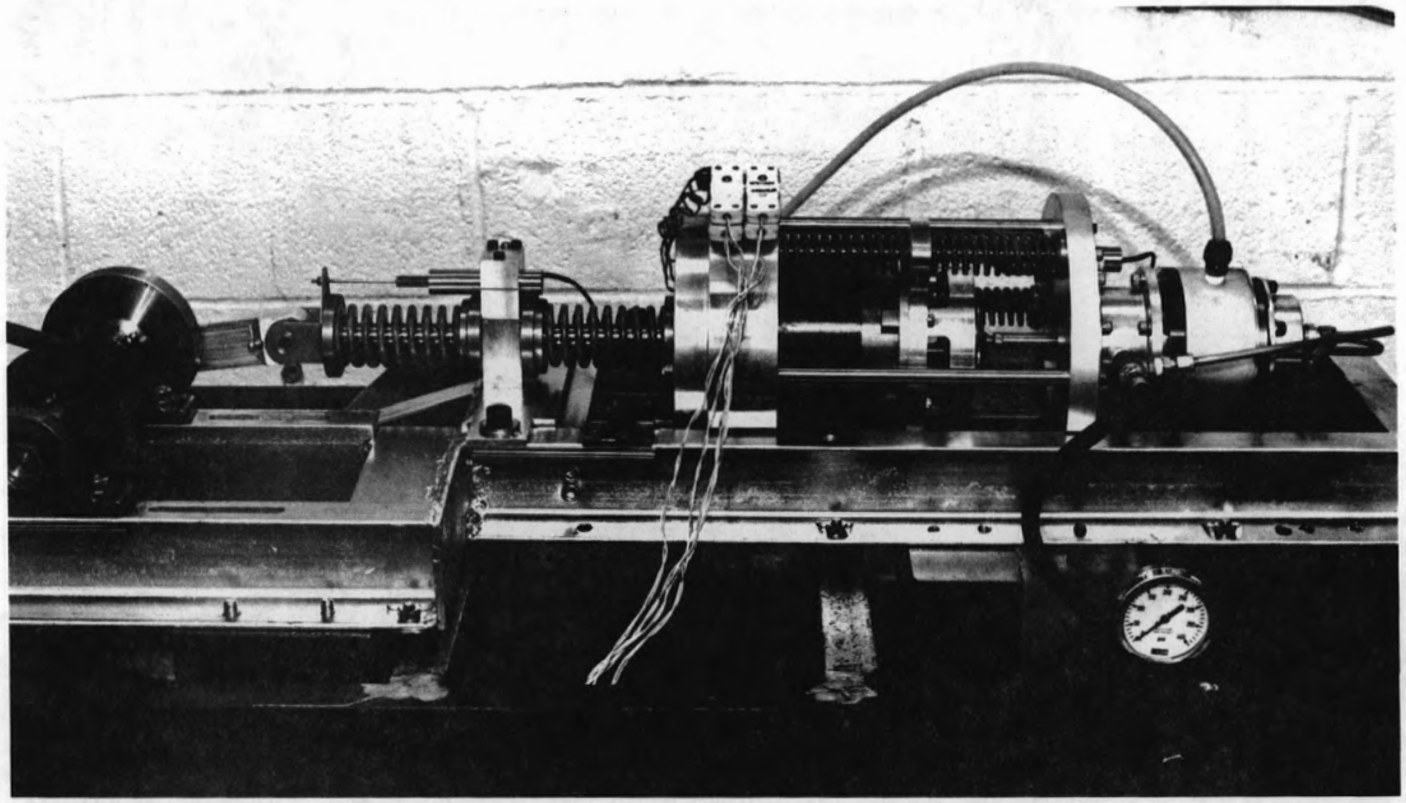

Figure 3.3 Magnetic Coupling/Double-Acting Compressor Assembly of Test Rig

The experimental magnetic coupling specifications are listed in Table 3.2. The gap, G, is usually a predetermined parameter in design. By considering the pressure of 2.5 MPa (25 bar) in the 3 kW air-charged FPSE, the required thickness of the 304 type stainless steel shell in the test assembly (Fig. 3.1) was determined to be 1.5 mm. Allowing a 0.9 mm clearance between the shell and the magnet rings on each side gave a G equal to 3.3 mm in the magnetic coupling design. Components of the magnetic coupling are shown in Fig. 3.4.

Table 3.2 Experimental Magnetic Coupling Specifications

The Number of Rings	6
Gap Between Inner and Outer Magnets (G) [mm]	3.3
Mean Diameter (D) [mm]	103.5
Magnet Ring Width (w) [mm]	12
Magnet Thickness (t_m) [mm]	5
Iron Base Thickness (t_b) [mm]	3.5
Axial Spacing Between Magnet Rings (d) [mm]	1
Stainless Steel Shell Thickness (t_s) [mm]	1.5

The double-acting test compressor, (see Fig. 3.5), could provide not only loading, but also spring effect to the magnetic coupling at both back and forth stroke. In test, the compressor was cooled by water flowing through a housing outside the compressor cylinder.

Displacements of the inner and outer coupling components were measured during operation by fast linear displacement transducers (FLDT) with high accuracy and very low phase shifts [8], thus giving the coupling deflection. The axial force on the magnetic coupling could be evaluated from the force-deflection relationship. The temperature of the stainless steel shell and the aluminum bearing support were measured by

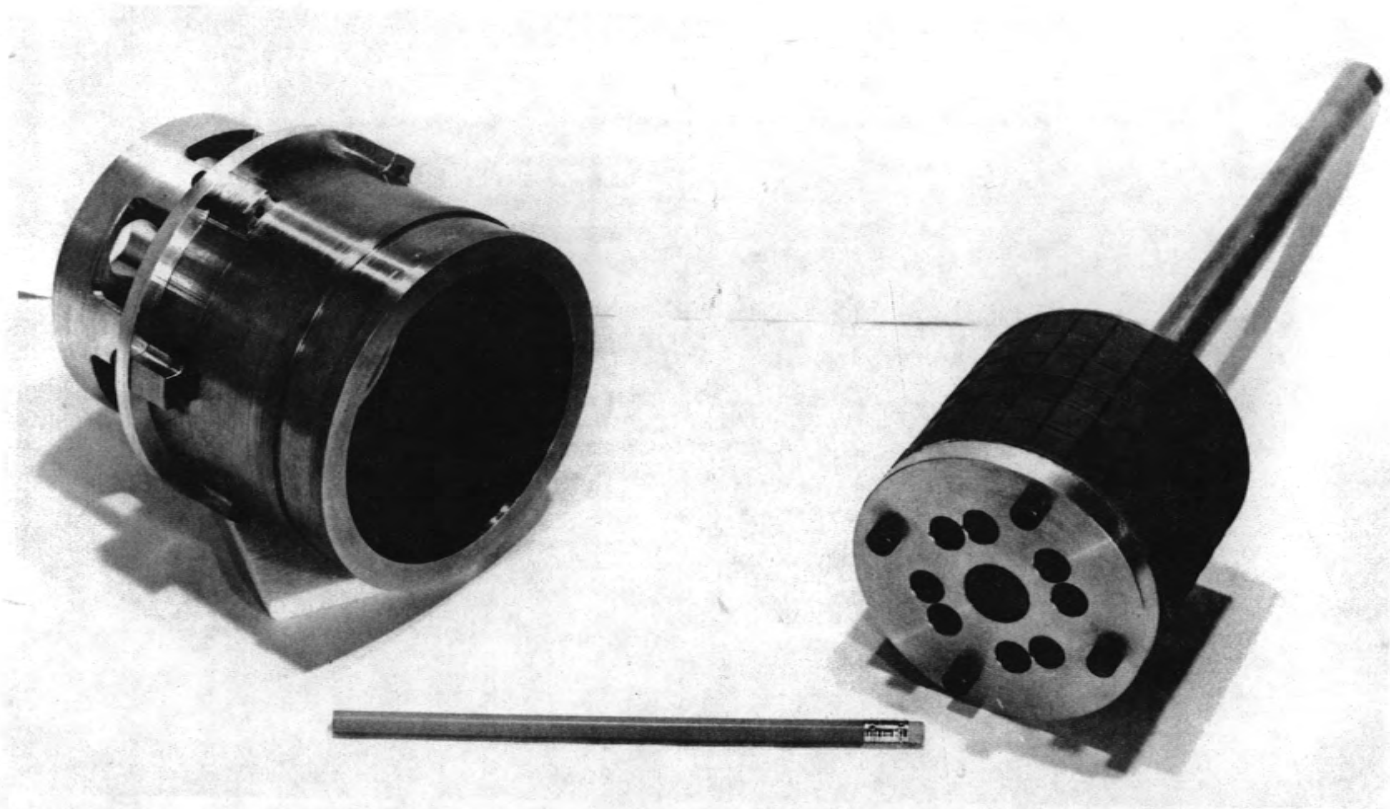

Figure 3.4 Coupling Components

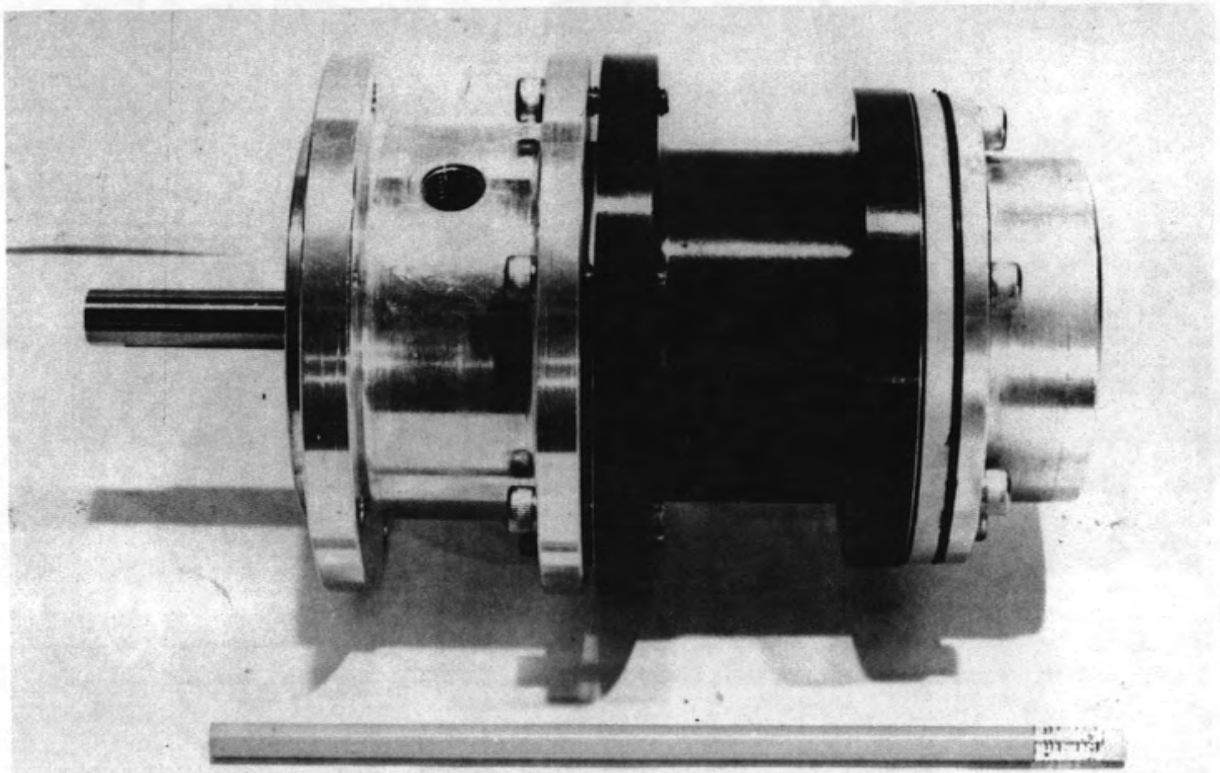

Figure 3.5 Double-Acting Test Compressor

thermocouples; and the temperature of the magnet and iron stator were measured by temperature indicator labels mounted on the surfaces of the magnet and iron stator.

3.2 Tests and Result Analyses

The test rig was first operated at 15 Hz and 35 Hz without a spring applied to the driven components and at 58 Hz with springs installed on the driven components. (See Section 3.2.3 for an explanation of the 58 Hz operation.) In all the tests, the double-acting compressor was loaded by air discharged through a pressure-controlled valve to a pressure tank. Since the Phase I testing program concentrated on evaluation of the magnetic coupling, the compressor did not run under a refrigerant load. The completed tests and test results with analyses are summarized in the following sections.

3.2.1 Magnets Exposed to R-22

Since the permanent magnets in a magnetic coupling used in a hermetically sealed FPSE magnetically coupled heat pump would be exposed to the refrigerant, this test was performed to assess the physical behavior of the magnets after exposure to liquid R-22.

The experimental procedure and results are as follows:

Magnets measuring $12 \times 12 \times 5$ mm (Neodymium Iron-Hicorex Nd 94 EB from Hitachi) were put into a pressure tank containing liquid R-22 for 21 days. During this period the tank was heated 10 times to about 60°C and kept at this temperature for 40 minutes each time. There was no detected difference in the physical appearance and magnetic properties of the magnets after the test. Magnets can also be coated with material such as epoxy for protection from the working fluid.

3.2.2 Force-Deflection Characteristic of the Experimental Coupling

The load on the magnetic coupling is only the compressor damping force in an ideal design. As previously described, the load on the magnetic coupling for a refrigerant

compressor could be simply represented by the load from the equivalent air compressor in the test program. The force-deflection characteristic (static behavior) of the experimental magnetic coupling in the test rig was measured and the results are plotted in Fig. 3.6. For comparison, results calculated from the analytical model, shown in Fig. 2.2, are plotted in Fig. 3.6 (Also, see Table 3.3.). Conclusions from this test are:

1. The analytical model can accurately predict the linear magnetic coupling characteristics since the results of the analytical model and the tests are consistent in the region of operating conditions ($x<x|_{dF/dx=0}$).

2. The load capacity of a magnetic coupling can be simply evaluated from its force-deflection characteristics. The only force which must be transmitted by an ideally designed magnetic coupling is the damping force. The maximum damping force of a double-acting compressor can be calculated from equation (2.3).

Table 3.3 Axial Force of the Test Magnetic Coupling as a Function of its Deflection

x (mm)	1.2	2.4	3.6	4.8	6.0	7.2	8.4	9.6	10.8
F_m (N)	889	1,689	2,334	2,801	3,112	3,246	3,179	2,934	2,500
F_a (N)	960	1,807	2,470	2,920	3,153	3,169	2,979	2,560	1,945

The maximum damping force of a double-acting compressor, running at 60 Hz and 30 mm stroke with 3 kW dissipated power, is about 1,100 Newtons. The deflection of the experimental magnetic coupling under this load is shown in Fig. 3.6 as a mark on the measured curve. Thus, this magnetic coupling can transmit a power greater than 3 kW at 60 Hz and 30 mm stroke. In other words, a magnetic coupling for 3 kW power transmission, by containing fewer magnets,will be even smaller than that used in the test model.

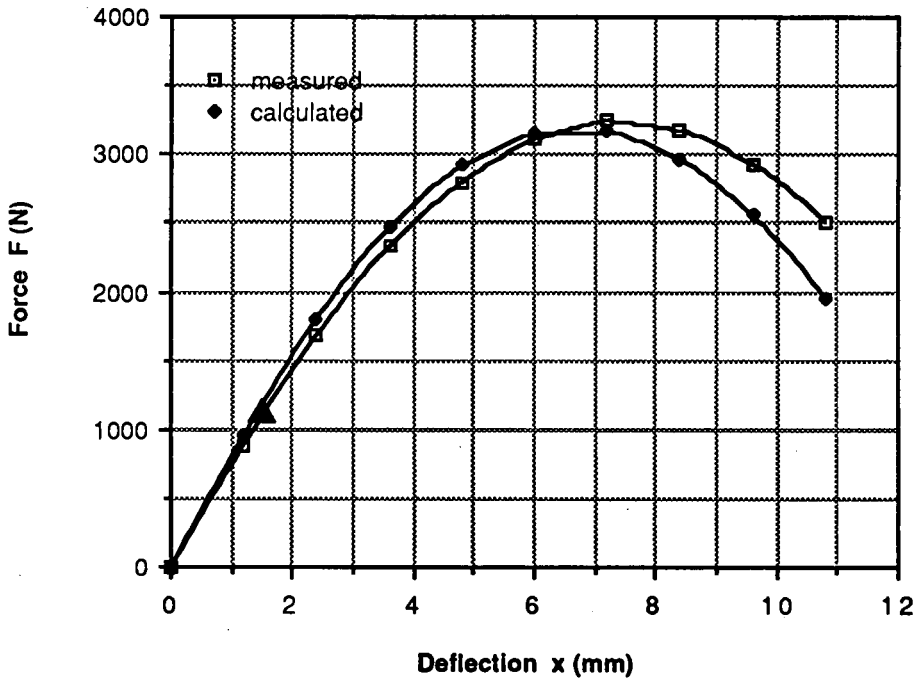

▲ maximum double-acting compressor damping force
(3 kW, 60 Hz, 30 mm stroke)

Figure 3.6 Force-Deflection Diagram of the Experimental Magnetic Coupling

3.2.3 System Operation

The test rig was operated at its maximum speed (58 Hz) after a minimum speed (15 Hz) and a low-speed operation (35 Hz). The maximum speed was measured during operation. The nominal design maximum frequency of the Sunpower 3 kW air-charged FPSE is 60 Hz.

The inertia force of the driven components is $X_c m_c \omega^2$. As the driven amplitude was treated approximately the same as the driving (12 mm) amplitude, the inertia force of the driven components of the test rig was about 320 N at 15 Hz and 1,750 N at 35 Hz, while it was about 4,800 N at 58 Hz. To maintain a tuned resonant system at high frequency (i.e., 58 Hz), added compensating springs were installed on the driven components. The system resonant characteristics have been previously described in Section 2.3.

3.2.4 Power Loss in a Magnetic Coupling

Representing heat generated within the shell, the power loss in a magnetic coupling can be expressed as the sum of two parts. One is heat stored within the shell, the other is heat transfer from the shell to the surroundings. Thus,

$$P_L = m_s c_s (dT_s/dt) + Q_s \tag{3.1}$$

where m_s is the mass of the shell with an axial length swept by the magnets, c_s is the specific heat of the shell material, T_s is the shell temperature, and Q_s is the heat transfer rate from the shell to its surroundings. Obviously, $Q_s \rightarrow 0$ as t (time)$\rightarrow$ 0 since the temperature gradient between the shell and its surroundings is negligible when the coupling first starts running. The loss can be written as a function:

$$P_L = m_s c_s (dT_s/dt) \mid_{t \rightarrow 0} \tag{3.2}$$

Therefore, the loss can be simply evaluated by measuring the instantaneous temperature-rise rate ($dT_s/dt) |_{t \to 0}$) of the shell at the moment the magnetic coupling starts running. For example, Fig. 3.7 depicts the temperature of the 304 type stainless steel shell within the coupling gap along with time within the starting period of the test rig's operation. The actual time interval of temperature measurements in this case was 3 seconds. With c_s = 480 J/kg°C for the 304 type stainless steel shell at room temperature, the loss calculated from equation (3.2) is about 220 W.

The loss of the magnetic coupling in the test rig oscillating at 58 Hz with varying piston strokes was evaluated in this way and plotted in Fig. 3.8. Results evaluated by the theoretical model are also shown in the same figure. The results on comparing tests and theory were:

1. Close agreement of the testing and calculated results (Fig. 3.8) indicates the loss for any particular design can be evaluated by the analytical model. For example, a properly designed magnetic coupling with a 100 mm diameter can link a 3 kW free-piston Stirling engine, with an internal pressure of 2.5 MPa (25 bar) and an operating frequency of 60 Hz, to a double-acting refrigerant compressor in a heat pump. The gap between the inner and outer magnetic rings (G) would be 3 mm and the thickness of the stainless steel engine pressure vessel (t_s) within the gap would be 1.4 mm, which is strong enough to bear the engine internal pressure. For the neodymium iron used in this example, B_r is 1.05 T, and the coupling loss, as determined from Fig. 3.9 for the 3 kW air-charged engine running at 60 Hz and 30 mm stroke, would be about 190 W (6.3 percent of 3 kW).

2. To reduce the hysteresis loss, materials with both high electrical resistivities and high strengths, like titanium alloys, should be used to make the pressure vessel. As shown in Fig. 2.3, the coupling loss rapidly decreases as the electrical resistivity increases.

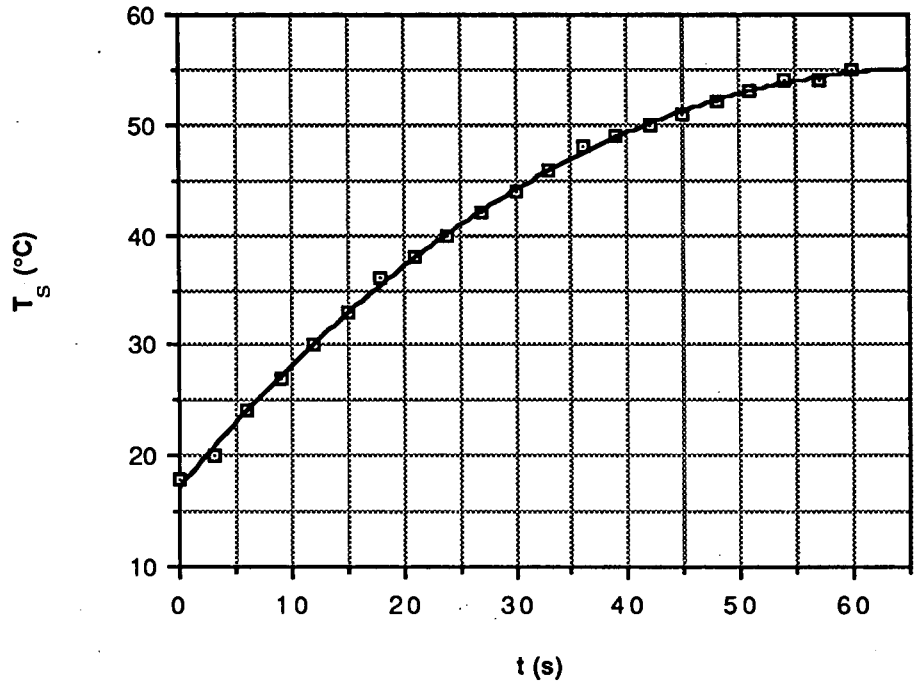

$T_s = 18.0 + 1.19\ t - 0.01\ t^2 + \ldots\ldots\ldots$ HOT

T_s - temperature of the stainless steel shell

t - operating time

HOT - higher order terms

Figure 3.7 Stainless Steel Shell Temperature within a Starting Period of the Test Rig Operation (58 Hz, 22 mm Driven Stroke)

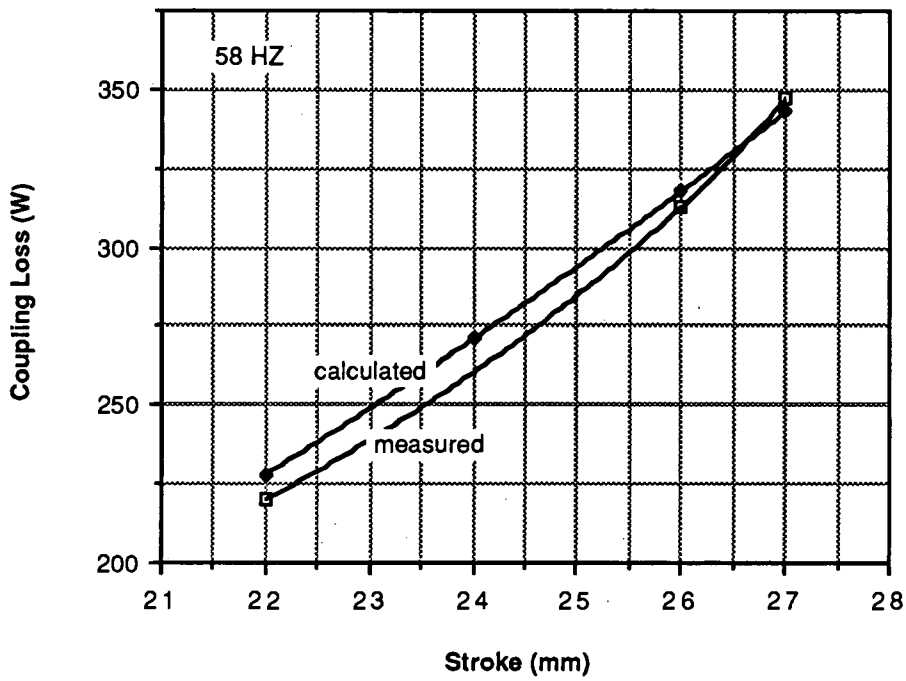

Stroke - stroke of the driven component

Figure 3.8 Power Loss in the Experimental Magnetic Coupling

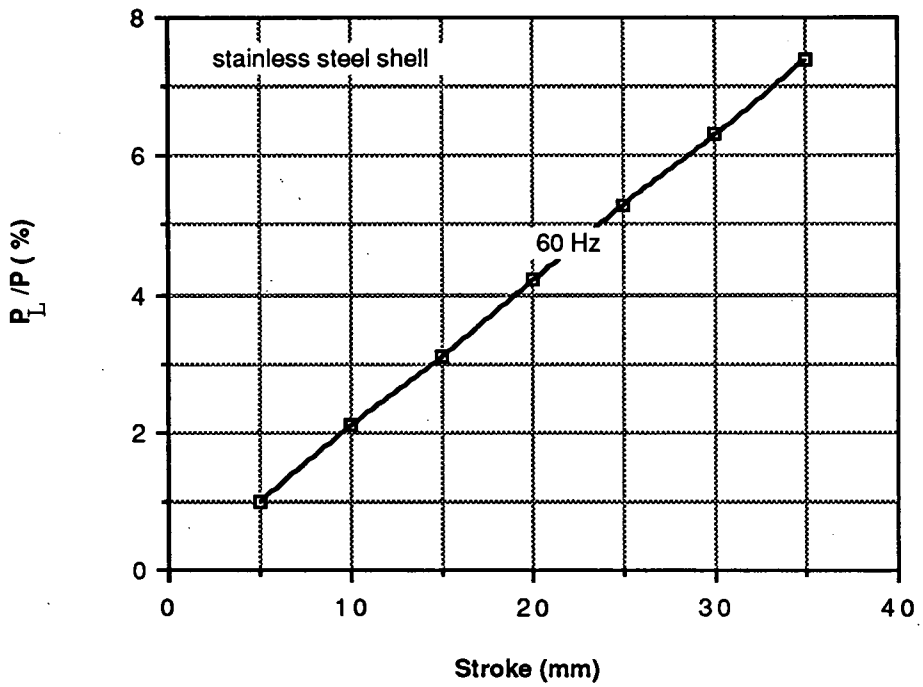

P - power input

P_L - power loss

Figure 3.9 Predicted Power Loss in an Ideally Designed Magnetic Coupling to be Used for a 3 kW Engine with Various Strokes (Neodymium Iron; 2.5 MPa; G ~ 3 mm)

Gap

3.2.5 Operating Temperature of a Magnetic Coupling

Since magnetization loss in a permanent magnet occurs as the temperature of the magnet increases, the operating temperature of a magnetic coupling is a concern in the design. Several thermocouples were installed on the stainless steel wall and temperature labels were stuck on the magnet surface at various locations. The stainless steel wall temperature along with the test rig running time is shown in Fig. 3.10.

As previously described, the power loss in a magnetic coupling can be expressed as:

$$P_L = m_s c_s (dT_s/dt) + Q_s$$

$$= m_s c_s (dT_s/dt) + A\ U\ \Delta T_s \qquad (3.3)$$

where A is the shell surface area, U is the overall heat transfer coefficient of the surface to the surroundings, and ΔT_s is the temperature difference between the shell and the surroundings. Since the average slope of (dT_s/dt) at any time interval may be found from Fig. 3.10, and the surrounding temperature was 18°C, the power loss is:

$$P_L = m_s c_s (55\text{-}18) + A\ U\ [(55+18)/2 - 18] \quad \text{for } 0 < t < 1 \text{ (min), and}$$

$$P_L = m_s c_s (105 - 103)/4 + A\ U\ [(105+103)/2 - 18] \quad \text{for } 33 < t < 37 \text{ (min)}$$

By simply treating U as a constant, by substituting $AU/m_s c_s$ found from solving the above simultaneous equations into (3.3), and by setting $(dT_s/dt) = 0$, equation (3.3) gives:

$$\Delta T_s \,|_{dT_s/dt=0} = 87\ ^\circ\text{C and}$$

$$T_s \,|_{dT_s/dt=0} = 87+18 = 105\ ^\circ\text{C}$$

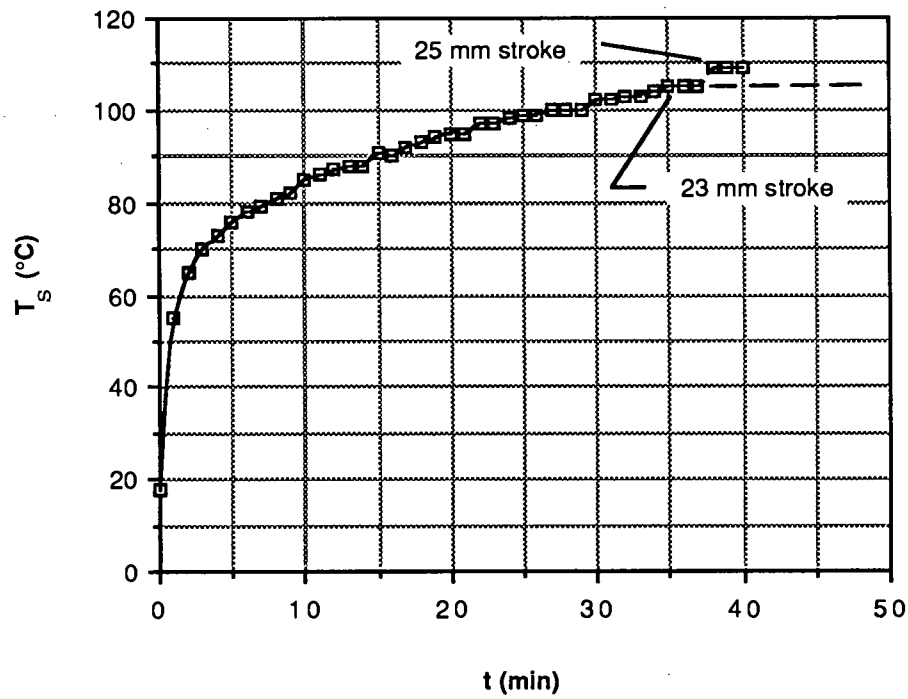

T_s - temperature of the stainless steel shell

t - operating time

Stroke - driven components

Figure 3.10 Operating Temperature of Stainless Steel Shell in the Experimental Magnetic Coupling (58 Hz)

where $dT_s/dt = 0$ means the shell temperature reaches a stable value.

Compared with $T_s \mid_{t=37\ min} = 105°C$ which is shown in Fig. 3.10, the result above indicates that after the test rig operates for 37 minutes the temperature nearly stabilizes. This can also be explained physically as follows: At a certain temperature, the loss will entirely go to the surroundings as the heat transfer from the shell. Under this stable condition, the measured magnet surface temperature ranged from 85°C to 90°C, which is within the recommended operating temperature range for neodymium iron.

It is noted that the last three data points in Fig. 3.10 show a temperature jump. This was caused by a coupling loss increase when the driven stroke was suddenly changed from 23 mm to 25 mm, proving again that the loss was related to the factors included in the analytical calculation.

The operating temperature of a magnetic coupling depends on not only the loss, but also heat transfer from the coupling to the surroundings. Any arrangement that improves the heat transfer can lower the operating temperature.

3.2.6 Irreversible Loss

The irreversible loss of neodymium iron magnets at the operating temperature was evaluated by comparing the force given by the coupling before and after the 40 minute operation. Its measured F-x curves before and after the operation are shown in Fig. 3.11. No significant change was observed. Usually, the irreversible loss is small within the operating temperature range of magnets like those used in the experimental coupling.

The coupling design should include consideration of the permanent magnet reversible loss due to a temperature elevation during operation. For the magnets used in the experimental coupling, the reversible temperature coefficient of magnetization is

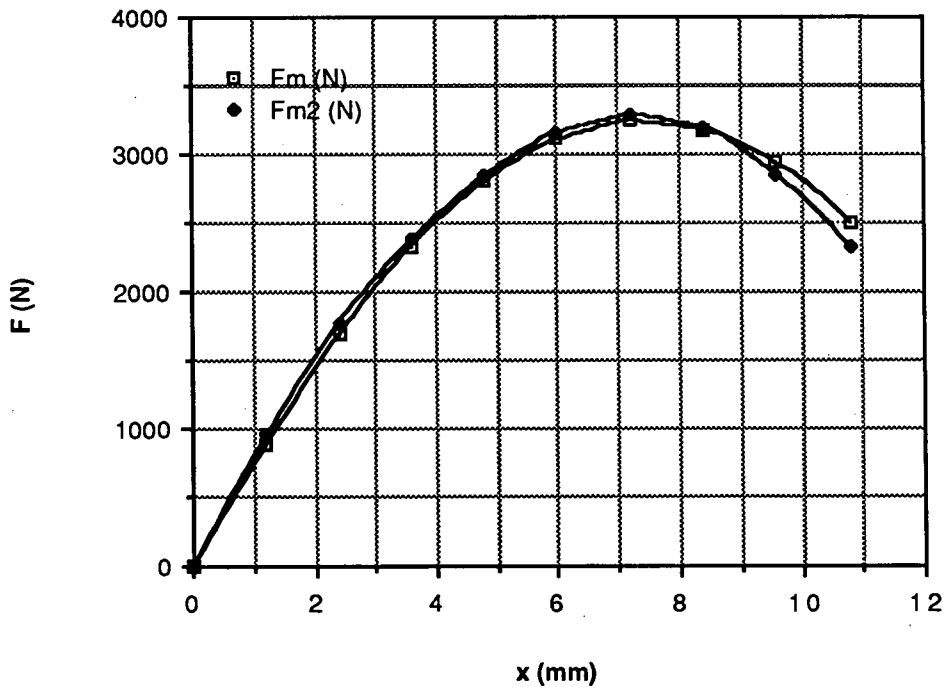

Fm - before operation

Fm2 - after operation

Figure 3.11 Static Force-Deflection Diagram of the Experimental Magnetic Coupling Before and After Operation

-0.109% / °C (see Table 3.1). This indicates that the magnets will be demagnetized by about 7 percent as the magnet temperature rises from room temperature to 85°C. Any way, to limit both the reversible and irreversible loss of neodymium iron used in a magnetic coupling, consideration of making the magnet temperature rise as small as possible should be taken in design.

3.2.7 Rotational Force and Side Loading

The side load of a magnetic coupling greatly depends upon the eccentricity of the magnetic pairs. The side load of the coupling used in the test rig as a function of eccentricity was predicted by the analytical model as shown in Fig. 3.12. However, both the side load and rotational force are negligible when the coupling components are within usual machining tolerances.

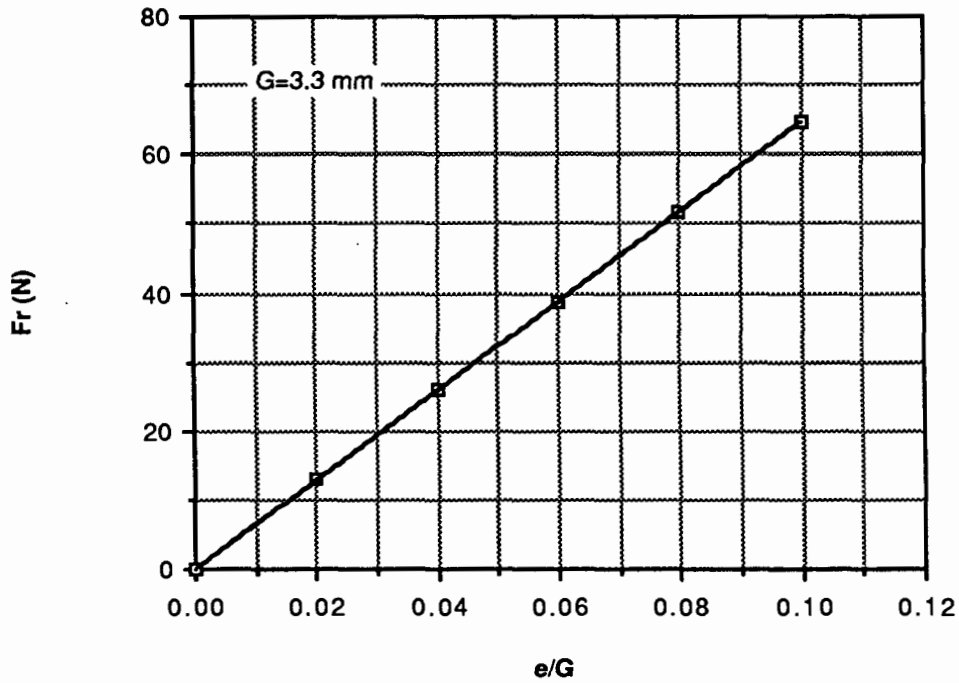

e / G - eccentricity/coupling radial gap

Figure 3.12 Predicted Radial Force of the Experimental Magnetic Coupling along with Eccentricity of Magnet Pairs (Static Condition)

4.0 FPSE/MAGNETIC COUPLING/COMPRESSOR ASSEMBLY

The 3 kW air-charged FPSE previously developed by Sunpower was proposed for heat pump assembly evaluation. Therefore, based on successful completion of the coupling effort, a preliminary design of a FPSE/magnetic coupling/compressor (FPSE/MC/C) assembly was prepared as an application of the 3 kW air-charged engine [9]. Some specifications of the preliminary design are shown in Fig. 4.1 and Table 4.1.

Table 4.1 Assembly Design Specifications

Engine Output Power	3 kW
Engine Working Gas	Air
Engine Mean Pressure	2.5 MPa
Frequency	60 Hz
Power Piston Stroke	30 mm
Compressor Type	Double-Acting
Refrigerant	R-22

The system operating frequency of 60 Hz is identical with the electricity supply. A linear alternator with battery can be used as a motor to start the engine and as a generator to supply electrical power to auxiliary equipment, such as a burner blower and water pump. This could make the heat pump system independent of an outside electrical power supply.

The determination of coupling-design parameters is based on the analytical design model and previous test results. The required magnet mass for an ideally designed magnetic coupling with a fixed load capacity and a given G is inversely proportional to the product of the operating frequency and stroke. As an example, the magnet mass of a magnetic coupling for a FPSE/double-acting compressor assembly (2.5 MPa internal pressure, 60 Hz operating frequency, and stainless steel pressure vessel) was evaluated and the

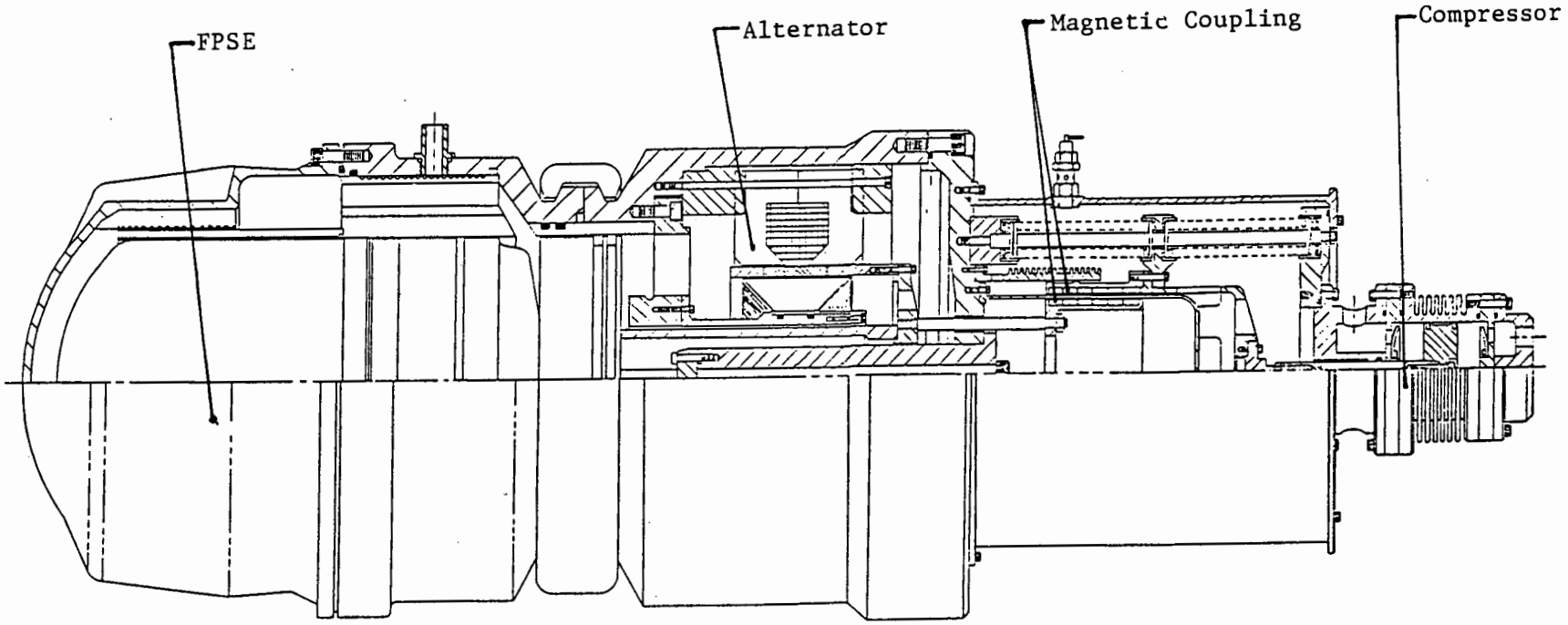

Figure 4.1 Air-Charged FPSE/Magnetic Coupling/Compressor Assembly (Preliminary, 3kW)

results are shown in Fig. 4.2. Due to the 30 mm stroke and 2.5 MPa pressure of the 3 kW air-charged engine, the magnet mass for a magnetic coupling using a double-acting compressor will be about 0.8 kg.

The inner coupling rings are contained in a stainless steel cylindrical shell which will be part of the engine pressure vessel. The driven components will be tuned by applying mechanical springs.

It is noted that the 3 kW air-charged engine was originally developed at Sunpower for a Stirling/generator application. This section gives a design concept of a FPSE/MC/C assembly using the air-charged engine only. In the design shown in Fig. 4.1, the linear alternator remains in the engine pressure vessel and a refrigerant compressor, a magnetic coupling, and mechanical springs are added to the engine at its lower end.

An assembly design with a free-piston Stirling engine particularly for the heat pump application is under consideration. This engine will use helium as the engine working fluid and its configuration will be much more compact. This design will be described in the Phase IIA final report.

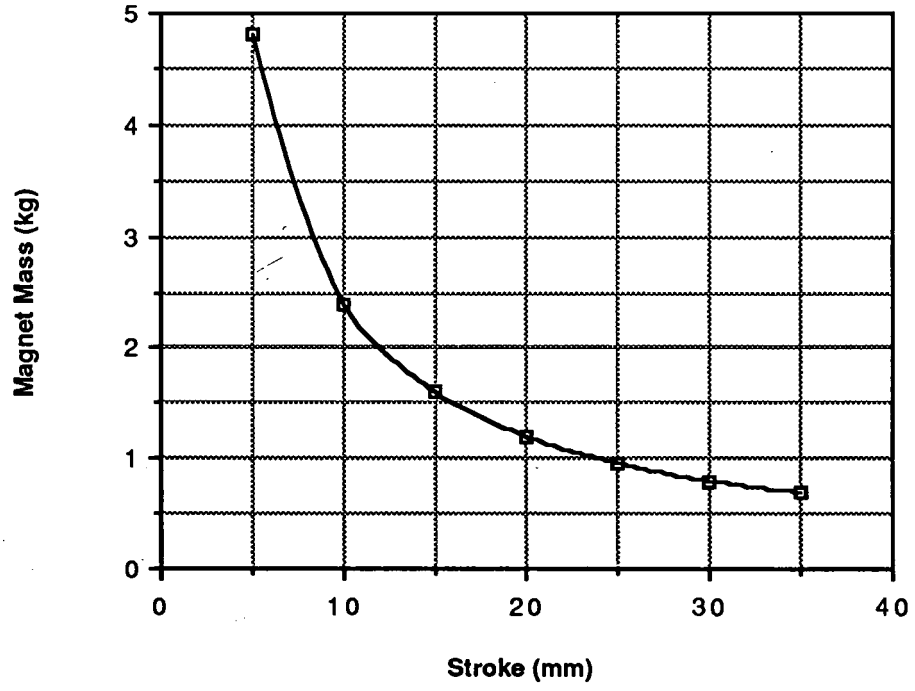

Stroke - driven components

Figure 4.2 Required Magnet Mass of a Coupling Linked to a Double-Acting Compressor (P=3 kW, G=3 mm, f=60 Hz, Neodymium Iron)

5.0 REFERENCES

1. Arthur D. Little, Inc., "Status of Free-Piston Stirling Engine Driven Heat Pump Development, Issues, and Options," ORNL/Sub/84-00205/1, April 1986.
2. Chen, G., Redlich, R. and Shade, D., "Evaluation of A Magnetic Coupling for Hermetic Power Transmission in a Stirling-Rankine Heat Pump," Paper No. 889040, Proc. 23rd IECEC, August 1988.
3. Chen, G. and Beale, W.T., "Magnetically Linked Free-Piston Stirling-Refrigerant Compressor Heat Pump," Proc. ASME Winter Annual Meeting, AES-Vol. 8 / SED-Vol. 6 (Book No. G00453), pp. 57-60, 1988.
4. "Magnet Catalog P5A," Permag, 1986.
5. "INCOR & NeIGT," I G Technologies, Inc.
6. Kraus, J.D. and Carver, K.R., "Electromagnetics," Second Edition, McGraw-Hill, 1973.
7. "Magnet Catalog P5A," Permag, p. 17, 1986.
8. "The FLDT, A Fast Linear Displacement Transducer;" Sensors, pp. 47-49, September 1987.
9. Berchowitz, D.M., Richter, M. and Shade, D., "Development and Performance of a 3 kW(e) Air-Charged Free-Piston Stirling Engine with Linear Alternator," Paper No. 879216, Proc. 22nd IECEC, pp. 1835-1840, August 1987.

ORNL/Sub/86-SA578/1
Dist. Category UC-95d

INTERNAL DISTRIBUTION

1. F. C. Chen
2. F. A. Creswick
3. R. C. DeVault
4. P. D. Fairchild
5. S. K. Fischer
6-11. A. F. Frederick
12. W. Fulkerson
13. P. J. Hughes
14. M. A. Kuliasha
15. R. W. Murphy
16. E. T. Rogers
17-21. M. O. Saunders
22. R. B. Shelton
23-27. J. A. Shonder
28. T. J. Wilbanks
29. S. J. Wolfe
30. A. W. Trivelpiece
31-32. Central Research Library
33. Document Reference Section
34-35. Laboratory Records-RC
36. ORNL Patent Office

EXTERNAL DISTRIBUTION

37. R. A. Ackermann, General Electric Co., R&D Center, P. O. Box 43 Schenectady, NY 12301
38. William Beale, Sunpower, Inc., 6 Byard Street, Athens, OH 45701
39. Glendon M. Benson, Energy Research and Generation, Inc., Lowell and 57th Streets, Oakland, CA 94608
40. Don Beremand, NASA-Lewis Research Center, 21000 Brookpark Road, Cleveland, OH 44135
41. Dick Bloomquist, Code 2752, David W. Taylor Naval Ship R&D Center, Annapolis, MD 21402
42. T. A. Braun, Tectonics Research, Inc., 9556 West Bloomington Freeway, Minneapolis, MN 55431
43. J. P. Budliger, Battelle-Geneva, 7 route de Drize, 1227 Carouge (Geneva), SWITZERLAND
44. J. G. Carbonell, Associate Professor of Computer Science, Carnegie-Mellon University, Pittsburg, PA 15213
45. Stig C. Carlqvist, Societe ECA, Boite Postale 16, 92194 Meudon Cedex, FRANCE
46. Dick Cawley, Lennox Industries, Inc., 1600 Metrocrest Drive, Carrollton, TX 75006
47. M. Clinch, Gas Research Institute, 8600 West Bryn Mawr Avenue, Chicago, IL 60631
48. E. H. Cooke-Yarborough, Lincoln Lodge, Longworth Nr Abingdon, Oxfordshire, OX13, 5DU, ENGLAND
49. J. J. Cuttica, Vice President of Research and Development, Gas Research Institute, 8600 W. Bryn Mawr Avenue, Chicago, IL 60631
50. J. G. Daley, Argonne National Laboratory, 9700 South Cass Avenue, Argonne, IL 60439
51. D. K. Darooka, General Electric Company, P.O. Box 527, King of Prussia, PA 19406
52. R. L. Demler, Foster-Miller Associates, Inc., 350 2nd Avenue, Waltham, MA 02254

53. G. R. Dochat, Mechanical Technology, Inc., 968 Albany-Shaker Road, Latham, NY 12110
54. J. E. Dudenhoefer, NASA-Lewis Research Center, 21000 Brookpark Road, Cleveland, OH 44135
55. T. Finkelstein, Stirling Associates International, P.O. Box 643 Beverly Hills, CA 90213
56. R. J. Fiskum, Energy Conversion Equipment Branch, CE-132, 5H-048/FORS, U.S. Department of Energy, 1000 Independence Avenue SW, Washington, DC 20585
57. M. Foster, Homach Systems, Ltd., Hargraves Road, Groundwell Industrial Estate, Swindon Wilts, SN2, 5AZ, ENGLAND
58. A. A. Frank, Mechanical Engineering Dept., University of California of Davis, Davis, California 95616
59. S. Freedman, Gas Research Institute, 8600 West Bryn Mawr Avenue, Chicago, IL 60631
60. D. R. Gedeon, Gedeon Associates, Box 141 A, South Canaan Road, Athens, OH 45701
61. Ted Gilles, Lennox Industries, Inc., Promenade Towers, P.O. Box 400450, Dallas, TX 75240
62. S. M. Gillis, Dean of the Graduate School, Duke University, 4875 Duke Station, Durham, NC 27706
63. L. Goldberg, University of Minnesota, Department of Civil and Mineral Engineering, 500 Pillsbury Drive SE, Minneapolis, MN 55455
64. B. S. Goldwater, Mechanical Technology, Inc., 968 Albany-Shaker Road, Latham, NY 12110
65. Sigmunel Gronich DOE Solar, CE-331, 5H/FORS, 1000 Independence Avenue, SW, Washington, DC 20585
66. A. C. Harvey, Foster-Miller Associates, Inc., 350 2nd Avenue, Waltham, MA 02254
67. Bob Holtz, Argonne National Laboratory, 9700 South Cass Avenue, Argonne, IL 60439
68. R. C. Hundt, Lennox Industries, Inc., 1600 Metrocrest Drive, Carrollton, TX 75006
69. P. Huntley, Borg-Warner Research, 1200 South Wolf Road, Des Plaines, IL 60018
70. B. C. Hwang, Code 2722, David Taylor Naval Ship R&D Center, Annapolis, MD 21402
71. H. S. Izawa, Washington Gas Light Company, Research Department, 6801 Industrial Road, Springfield, VA 22151
72. F. R. Kalhammer, Vice President, Electric Power Research Institute, P.O. Box 10412, Palo Alto, CA 94303
73. J. P. Kalt, Professor of Economics, Kennedy School of Government, Harvard University, 79 John F. Kennedy Street, Cambridge, MA 02138
74. T. Kapus, CE-113, Building Equipment Division, U.S. Department of Energy, 1000 Independence Avenue SW, Washington, DC 20585
75. K. P. Lee, Aspen Systems, Inc., 275 Boston Post Road, Marlborough, MA 01752
76. Bengt Lindquist, Swedish Council for Building Research, Sankt Goransgatan 66, S-11233 Stockholm, SWEDEN
77. R. J. Meijer, Stirling Thermal Motors, Inc., 2841 Boardwalk, Ann Arbor, MI 48104
78. A. Mitsuda, New Energy Development Organization, Sunshine 60 29F, 101 3-Chome Higashi-Ikebukuro, Toshima-Ku, Tokyo 170 JAPAN

79. D. E. Morrison, Professor of Sociology, Michigan State University, 201 Berkey Hall, East Lansing, MI 48824-1111
80. G. Myers, Gas Research Institute, 8600 West Bryn Mawr Avenue, Chicago, IL 60631
81. N. P. Nightingale, Mechanical Technology, Inc., 968 Albany-Shaker Road, Latham, NY 12110
82. Herbert Nilsson, United Stirling AB, P.O. Box 856, S-201 80 Malmo, SWEDEN
83. W. H. Percival, United Stirling, Inc., 1800 Diagonal Road, Alexandria, VA 22314
84. R. L. Perrine, Professor, Engineering and Applied Sciences, Civil Engineering Department, Engineering I, Room 2066, University of California, Los Angeles, CA 90024
85. B. Qvale, Laboratory for Energetics, The Technical University of Denmark, DTH Building 403, DK-2800 Lyngby, DENMARK
86. E. A. Reid, Jr., Columbia Gas System Service Corporation, 1600 Dublin Road, Columbus, OH 43215
87. P. Riggle, Joint Center for Graduate Study, University of Washington, 100 Sprout Road, Richland, WA 99352
88. T. Roose, Gas Research Institute, 8600 West Bryn Mawr Avenue, Chicago, IL 60631
89. J. D. Ryan, Energy Conversion Equipment Branch, CE-132, 5H-048/FORS, U.S. Department of Energy, 1000 Independence Avenue SW, Washington, DC 20585
90. J. G. Schreiber, NASA-Lewis Research Center, 21000 Brookpark Road, Cleveland, OH 44135
91. J. R. Senft, Department of Mathematics/Computer Science, University of Wisconsin, River Falls, WI 54022
92. J. G. Slaby, NASA-Lewis Research Center, 21000 Brookpark Road, Cleveland, OH 44135
93. J. L. Smith, Jr., Mechanical Engineering Department, Massachusetts Institute of Technology, Cambridge, MA 02139
94. P. F. Swenson, The East Ohio Gas Company, East 9th Avenue at Superior, P.O. Box 5759, Cleveland, OH 44101
95. W. P. Teagan, Arthur D. Little, Inc., 20 Acorn Park, Cambridge, MA 02140
96. R. C. Tew, NASA-Lewis Research Center, 21000 Brookpark Road, Cleveland, OH 44135
97. W. M. Toscano, Aspen Systems, Inc., 275 Boston Post Road, Marlborough, MA 01752
98. V. J. Van Griethuysen, Air Force Wright Aeronautical Laboratories, Wright-Paterson Air Force Base, OH 45433
99. D. A. Vaughn, ATTN: STRBE-EMP, Belvoir R&D Center, Ft. Belvoir, VA 22060
100. W. Waldron, Mechanical Technology, Inc., 968 Albany Shaker Road, Latham, NY 12110
101. G. Walker, University of Calgary, Department of Mechanical Engineering, 2500 University Drive NW, Calgary, CANADA T2N1N4
102. B. P. Wang, Mechanical Engineering Department, University of Texas at Arlington, P.O. Box 19023, Arlington, TX 76019
103. M. A. White, University of Washington, Joint Center for Graduate Study, 100 Sprout Road, Richland, WA 99352
104. L. Williams, Logan Lewis Library, Research Division, Carrier Corporation, Carrier Parkway, Syracuse, NY 13221

105. Ted Williams, Stirling Power Systems, 7101 Jackson Road, Ann Arbor, MI 48103
106. J. Wurm, Institute of Gas Technology, 3424 South State Street, Chicago, IL 60616
107. Institute for Energy Analysis, ORAU Library, Oak Ridge, TN 37831
108. Office of the Assistant Manager for Energy R&D, U.S. Department of Energy, Oak Ridge Operations, P. O. Box 2001, Oak Ridge, TN 37831-8600

109-333. Given distribution for Category UC-95d

☆U.S. GOVERNMENT PRINTING OFFICE 1989—648-119/00059